Chemical Geology 340 (2013) 151–161

Contents lists available at SciVerse ScienceDirect

Chemical Geology

journal homepage: www.elsevier.com/locate/chemgeo

# Selenium incorporation into calcite and its effect on crystal growth: An atomic force microscopy study

François Renard [a,b,c,*], German Montes-Hernandez [a,b], Encarnación Ruiz-Agudo [d], Christine V. Putnis [e]

[a] Univ. Grenoble Alpes, ISTerre, BP 53, F-38041 Grenoble, France
[b] CNRS, ISTerre, BP 53, F-38041 Grenoble, France
[c] Physics of Geological Processes, University of Oslo, Oslo, Norway
[d] Department of Mineralogy and Petrology, University of Granada, Fuentenueva s/n 18071, Granada, Spain
[e] Institut für Mineralogie, Universität Münster, Corrensstrasse 24, 48149 Münster, Germany

ARTICLE INFO

*Article history:*
Received 16 July 2012
Received in revised form 28 December 2012
Accepted 29 December 2012
Available online 7 January 2013

Editor: J. Fein

*Keywords:*
Calcite
Atomic force microscopy
Crystal growth
Selenium

ABSTRACT

The atomic processes leading to calcite growth are still debated. The presence of foreign impurities in solution is known to change the rate of step propagation during growth as well as the growth mechanism. Among trace elements, selenium, in the form of oxyanions, can incorporate into the calcite structure by replacing the carbonate group. In the present study, we record the effect of organic and inorganic selenium on calcite growth at room temperature by using in-situ time-lapse atomic force microscopy (AFM) and we confirm the observations by performing batch reactor experiments. Our results show that the incorporation of Se(IV) during calcite growth could be observed in-situ and the presence of this element modifies the morphology of growth features formed on a cleaved calcite surface, transforming typical pyramidal spiral growth hillocks into more complex heart-shape and tear-shape patterns. This effect is reversible as changing the solution back to a selenium-free composition recovers the original hillock pattern. Conversely, Se(VI) does not incorporate, but catalyzes the step propagation rate without changing the growth pattern. We have also observed that the presence of organic selenium (Se(−II)), in the form of seleno-L-cystine, has an effect on the nucleation of calcite crystals and their aggregation in clusters, but has no measurable effect on the morphology of growing steps at the calcite surface. These results indicate that calcite could represent a reservoir of selenite, whereas selenate would remain preferentially in solution, as observed in the composition of sea waters worldwide.



## 1. Introduction

Carbonate minerals are widespread at the surface of the Earth. They control the global carbon cycle by storing this element in various sedimentary formations. They also play a crucial role in the development of life by their presence in many living systems, from the shells of sea planktons to the bones of vertebrates. Among carbonates, calcite is the most common, shaping the surface of the Earth in many sedimentary basins and mountain ranges in the form of limestones and marbles. Understanding how calcite can nucleate and precipitate represents crucial challenges targeted since the 1970s' (Bischof, 1968; Nancollas and Reddy, 1971), including processes of biomineralization (Teng et al., 1998). However, a complete understanding of calcite growth processes, including trace element partitioning, at the atomic scale is still a challenging subject.

The study of calcite growth by direct in-situ observations provides valuable information on the detailed mechanisms of ion incorporation and how the complex structure of the calcite surface, with the presence of a large number of reactive sites (i.e. cleavage steps and kink sites), may control precipitation (Ruiz-Agudo and Putnis, 2012 and references therein). Such measurements also allow visualizing the effect of trace ions on the propagation of the calcite steps during growth and can help decipher whether trace elements either incorporate directly into calcite, or produce co-precipitates that would poison the calcite surface. For example, using a scanning force microscope, Dove and Hochella (1993) observed that phosphate modifies the geometry of the steps at the calcite surface, transforming relatively straight steps into jagged steps. The effects of ion activity ratio (Larsen et al., 2010) and the nature of the background ions in solution (Ruiz-Agudo et al., 2011) could be monitored at the atomic scale, providing useful insights necessary to link microscopic processes to macroscopic measurements of calcite growth. Under hydrothermal conditions (80–105 °C), it was possible to observe in situ, using an atomic force microscope (AFM), the growth of another carbonate, magnesite (Saldi et al., 2009) and measure the effect of fluid supersaturation on the growth rate of steps by a mechanism of hillock development similar to that of calcite.

The incorporation of impurities during calcite growth has been studied extensively (Staudt et al., 1994; Paquette and Reeder, 1995; Temman et al., 2000; Fujita et al., 2004; Lee and Reeder, 2006; Stipp

* Corresponding author at: Univ. Grenoble Alpes, ISTerre, BP 53, F-38041 Grenoble, France. Tel.: +33 476635907.
*E-mail address:* francois.renard@ujf-grenoble.fr (F. Renard).

0009-2541/$ – see front matter © 2013 Elsevier B.V. All rights reserved.
http://dx.doi.org/10.1016/j.chemgeo.2012.12.017

et al., 2006; Heberling et al., 2008; Ruiz-Agudo et al., 2011), as the presence of trace ions in the calcite structure could be used to infer past fluid circulations, fluid composition and degree of water-rock interaction. The incorporation of trace ions can lead to intersectoral zoning of the calcite crystals during growth, allowing probing the different surface sites and the controlling parameters of ion incorporation at the steps of the calcite surface (Staudt et al., 1994; Paquette and Reeder, 1995). The surface control is exerted by the presence of steps and kink sites at the calcite surface. For example, the incorporation of divalent ions with radii smaller than $Ca^{2+}$ is favored at steps that have smaller kink sites, whereas ions with larger radii are preferentially incorporated at less-constrained and larger kink sites. As a result, even if the composition of the fluid is homogeneous, the composition of the growing calcite can be heterogeneous when considering the incorporation of trace elements.

Among trace elements that may incorporate into calcite and change its growth rate, we focus here on how selenium oxyanions may incorporate or not into calcite during growth. Concerning selenate, different effects have been described (Reeder et al., 1994; Cheng et al., 1997; Montes-Hernandez et al., 2009). On the one hand, Reeder et al. (1994) proposed that Se(VI) could be incorporated into calcite, based on X-ray adsorption fine-structure XAFS spectroscopic studies and calculations of the distance between selenium atoms and their nearest atom neighbors. On the other hand, Montes-Hernandez et al. (2009) did not observe Se(VI) incorporation or adsorption, based on the solution analysis before and after calcite precipitation in batch reactors. Conversely, the incorporation of selenite Se(IV) could be observed under hydrothermal conditions, based on solution chemistry analysis and synchrotron extended X-ray adsorption fine-structure (EXAFS) spectroscopy (Montes-Hernandez et al., 2011).

Selenium is the element with the narrowest margin of concentration between essential and toxic effects. For example, dietary deficiency for humans occurs for consumption of selenium below 40 micrograms per day, whereas for concentration above 400 micrograms per day, it becomes toxic (Levander and Burk, 2006). As an example, the recommended European population intake is 55 micrograms per day (European Council Scientific Committee on Food, 2003). Ecotoxicological effects of selenium have been recognized for a long time (Draize and Beath, 1935; Ellis et al., 1937), with negative impact on living systems. Since then, this element has been largely studied because several environmental and health issues emerged due to the too low or too high consumption level by plants and animals, including humans, and its bioaccumulation in the food chains – see for example the review by Hamilton (2004).

Selenium is found in its natural form in volcanic rocks (Floor and Román-Ross, 2012), geothermal areas (Rouxel et al., 2004), coal (Yudovich and Ketris, 2006; Li and Zhao, 2007) and therefore potentially concentrated in mine waste, soils, waters and the atmosphere, and is transported in the environment (Malisa, 2001; Fernandez-Martinez and Charlet, 2009). The anthropogenic production of selenium, released into the atmosphere, is in the form of aerosols and dust and is mainly due to the industrial and domestic burning of coal, oil refinery and the pyrometallurgical production of several metals such a copper, nickel or zinc (Conde and Sanz Alaejos, 1997). This selenium is then delivered into soils during rain and snow precipitation. Another factor of selenium concentration in living systems is the use of seleniferous waters for irrigation in crop production leading to selenium oxyanion contamination in drainage waters and its accumulation in reservoirs (Mayland et al., 1989). Finally, Se-79 is a long lived (650000 years) radioactive mobile fission element, present in nuclear fuels and wastes resulting from reprocessing this fuel, and thus has the potential to contaminate the far-field environment around storage locations.

In the present study, we characterize how the presence of selenium, either inorganic and in two different oxidation states (selenite: Se(IV) and selenate: Se(VI)) or in an organic molecule (seleno-L-cystine: Se–Cys), modifies the growth of calcite. The direct effect of selenium on calcite growth was characterized using AFM imaging of calcite surfaces during precipitation and growth of pyramidal hillocks (spiral growth) studied at room temperature during flow-through experiments. The main result of this study is that inorganic selenite has a strong effect on calcite growth and is incorporated into the calcite crystal structure, presumably by replacing carbonate groups ($CO_3^{2-}$) by selenite groups ($SeO_3^{2-}$). This replacement has a strong effect on the morphology of precipitated calcite, transforming the pyramidal hillocks into heart-shaped forms. Conversely, selenate does not show any significant incorporation during calcite growth, but catalyzes the rate of step propagation. Finally, the organic selenium displays a complex effect. Only a small part of the selenite, produced by the chemical fragmentation of the Se–Cys, may be incorporated into the calcite. Moreover, the organic acid and amine groups may adsorb onto the calcite reactive surfaces and exert a control on the patterns of growing precipitates (Montes-Hernandez et al., 2011). All these AFM conclusions are confirmed by batch reactor experiments where calcite was synthesized at 30 °C in the presence of various concentrations of selenium. Direct observations have shown that Se(IV) can be incorporated into calcite, whereas Se(VI) is not, confirming the results presented by Montes-Hernandez et al. (2011). The new achievement in the present study is the direct observation, using AFM observations, of the effect of selenium on calcite growth at room temperature and the measurements of calcite precipitation rates at the atomic scale when varying the concentration of various selenium oxyanions in the fluid.

## 2. Materials and methods

### 2.1. Precipitation of calcite imaged using atomic force microscopy

For the AFM studies, solutions supersaturated with respect to calcite were prepared, to which selenium was added. $CaCl_2$ and $NaHCO_3$ 1 M stock solutions were prepared at room temperature (23 °C) from reagent grade sodium bicarbonate and calcium chloride salts that were dissolved into double-deionized water. The calcite growth solution was produced by mixing relevant proportions of these two stock solutions into double-deionized water. The pH of the solutions was close to 8.2 and the $Ca^{2+}/CO_3^{2-}$ ratio was equal to 1. The supersaturation of the solution was calculated as $\Omega = IAP/K_{sp} = 6.46$ where IAP is the ion activity product and $K_{sp}$ is the calcite solubility product, equal to $10^{-8.48}$ at 25 °C, based on the PHREEQC database (Parkhurst and Appelo, 1999). Growth solutions containing various concentrations of selenium (0.8, 4, 8, 40, 70, 200 and 400 ppm) were also prepared. The selenium was either inorganic (selenite $Na_2SeO_3.5H_2O$ or selenate $Na_2SeO_4$) or incorporated into an organic molecule, the seleno-L-cystine ($C_6H_{12}N_2O_4Se_2$). All chemical agents were obtained from Sigma Aldrich. The proportions of the various solutions (stock solutions and selenium solutions) were calculated using the PHREEQC software (Parkhurst and Appelo, 1999) and the concentrations are given in Table 1. Potential errors in the given concentrations come mainly from the 1 μL precision when sampling volumes of solutions.

Fresh calcite surfaces were prepared by cleaving a natural calcite (Iceland spar, Chihuahua, Mexico) along the $\{10\bar{1}4\}$ crystallographic plane, which because of its lowest atomic density represents a natural plane of weakness of the crystal. Time-lapse in-situ AFM observations of these calcite surfaces were performed using a flow-through fluid cell coupled to a Digital Instrument Nanoscope III multimode AFM (Bruker) working in contact mode at room temperature. Over the time-scale of the experiments, we assume that there would be no significant exchange between the fluid cell and the outside air. AFM images in the deflection mode were collected using $Si_3N_4$ tips (Veeco Instruments, tip model NP-S20) with spring constants 0.12 and 0.58 $N.m^{-1}$. The images were analyzed using the NanoScope software (Version 5.31r1) and exported into TIFF files that were processed using the Matlab software.

For each AFM experiment, a single calcite surface was studied in the following manner. Firstly, double-deionized water was flushed over the surface for several minutes to dissolve the first layers of calcite and adjust the parameters of the AFM. Then, the growth solution was injected from a syringe into the fluid cell which was sealed by an O-ring, allowing the reactive solution to flow over the calcite surface. Then time-lapse AFM scans were performed. During scans, no solution was passed over the calcite surface to avoid hydrodynamic perturbation of the AFM tip. Typical scans had surface areas of $4 \times 4$ to $10 \times 10$ μm, acquired at a scanning frequency of 2–4 Hz and a lateral pixel resolution in the range 15–40 nm. The scan duration was approximately 1.5 min. After each scan, the fluid in the flow cell was renewed, ensuring a constant fluid composition and supersaturation over the whole duration of the experiment. During an experiment, the fluid composition was changed, for example switching from growth using a selenium-free solution to growth in the presence of selenium. This was possible because of the fast reversibility of the growth process: changing the solution modified the growth pattern within minutes.

### 2.2. Method of analysis of angles and step velocities during calcite growth

The cleaved calcite surfaces show three main modes of growth that depend mainly on the supersaturation. Firstly, growth may occur through the propagation of steps emanating from growth islands that follow the rhombohedral morphology of calcite. Secondly, growth may occur by propagation of pre-existing steps. Thirdly, emergence of a screw dislocation at the cleavage surface provides a continuous source of steps and growth can occur by the formation of hillocks, also called pyramids or growth spirals (Paquette and Reeder, 1995; Ruiz-Agudo and Putnis, 2012).

The four edges observed on a calcite cleavage surface during growth or dissolution under normal conditions are parallel to $\left[\bar{4}41\right]_+$, $\left[48\bar{1}\right]_+$, $\left[\bar{4}41\right]_-$, and $\left[48\bar{1}\right]_-$ steps (Paquette and Reeder, 1995). During dissolution, the $\left[\bar{4}41\right]_-$ and $\left[48\bar{1}\right]_-$ steps are acute and intersect the bottom of the etch pit at an angle of 78°, while $\left[\bar{4}41\right]_+$ and $\left[48\bar{1}\right]_+$ steps are obtuse and intersect the bottom of the etch pit at an angle of 102° (Hay et al., 2003). Steps parallel to the same direction are not symmetrically equivalent. However, acute steps are structurally equivalent, as are obtuse steps. During growth, hillocks or pyramids formed around screw dislocations consist of growth layers each bounded by two obtuse and two acute step edges (Fig. 1a). The summit of the pyramid is off-centered and defines an angle $\varphi$ smaller than 180°. The base of the pyramid shows two acute and two obtuse angles, the latter ones defining an angle of 102°, typical of calcite. The hillock grows by the spreading of the four steps that have specific velocities ($v_{\text{obtuse}}$, $v_{\text{acute}}$) as defined in Fig. 1a. By measuring how a single step propagates in successive AFM images (Fig. 2), the two velocities can be calculated as following (Larsen et al., 2010; Ruiz-Agudo et al., 2011):

$$\begin{aligned} v_{\text{obtuse}} &= \sin\left(\frac{\varphi+\gamma}{2}\right)\frac{dx}{dt} \\ v_{\text{acute}} &= \sin\left(\frac{\varphi-\gamma}{2}\right)\frac{dx}{dt} \end{aligned} \quad (1)$$

where the angles $\varphi$ and $\gamma$ are defined on Fig. 1a, and the distance $x$ is shown to increase on Fig. 2, such that $\frac{dx}{dt}$ is the length variation of x divided by the time between two successive AFM scans.

### 2.3. Precipitation of calcite in batch reactors

In order to compare the above AFM experiments with batch reactor experimental results, the following set-up was repeated from Montes-Hernandez et al. (2011) and additional data were acquired. One liter of high purity water (electrical resistivity > 18.2 $m\Omega \cdot cm^{-1}$), 20 g of commercial portlandite $Ca(OH)_2$ (96% chemical purity, with 3% $CaCO_3$ and 1% other impurities, Sigma-Aldrich), and five different masses of sodium selenite pentahydrate or sodium selenate were placed in a stirred titanium reactor (Parr® autoclave) with an internal volume of 2 L. The aqueous suspension was well mixed by stirring (400 rpm). The reactor containing the aqueous dispersion (solution charged with Se oxyanion + $Ca(OH)_2$ particles in excess of its solubility) was then heated to 30 °C, and upon thermal stabilization, $CO_2$ (99.995% chemical purity, Linde Gas) was injected, until a $pCO_2$ of 20 bars was achieved ($pCO_2$ = total $P$ of system). At these $T$ and $P$ conditions, the vapor phase consists mainly of $CO_2$ gas in an ideal state. Here the $CO_2$ is the source of carbonation of the portlandite and its

**Table 1**
List of experiments: atomic force microscopy (AFM) and batch reactor studies. The supersaturation for AFM experiments has been calculated using PHREEQC. For the batch experiments, the supersaturation varies during the course of the experiment and the given value corresponds to a maximum supersaturation after ~3 min of reaction.

| AFM exp. # | Fluid composition ($\Omega = 6.46$, $Ca^{2+}/CO_3^{2-} = 1$) | Conditions |
|---|---|---|
| Se1 | Se(IV), 70 ppm | $P = 1$ bar, $T = 23$ °C |
| Se4 | Se(IV), 70 ppm | $P = 1$ bar, $T = 23$ °C |
| Se5 | Se (VI), 8 and 70 ppm, Se(IV), 70 ppm | $P = 1$ bar, $T = 23$ °C |
| Se6 | Se(IV) 0.8 ppm, 4 ppm, 8 ppm, 40 ppm | $P = 1$ bar, $T = 23$ °C |
| Se9 | Se–Cys (equiv. 70 ppm Se) | $P = 1$ bar, $T = 23$ °C |
| Se10 | Se(IV) 8 ppm, 200 ppm, 400 ppm | $P = 1$ bar, $T = 23$ °C |
| Se12 | Se(IV) 8 ppm, 200 ppm, 400 ppm, Se(VI) 60 ppm, 200 ppm, 400 ppm | $P = 1$ bar, $T = 23$ °C |
| **Batch exp. #** | **Fluid composition ($\Omega max = 1.3$, $Ca^{2+}/CO_3^{2-} = 0.33$)** | **Conditions** |
| Ref_Calcite #1 | Ca(OH)2-Water-$CO_2$ | $P = 20$ bar, $T = 30$ °C |
| Selenite–Calcite #2 | Se(IV), 0.24 ppm + Ref_Calcite solution #1 | $P = 20$ bar, $T = 30$ °C |
| Selenite–Calcite #3 | Se(IV), 16.32 ppm + Ref_Calcite solution #1 | $P = 20$ bar, $T = 30$ °C |
| Selenite–Calcite #4 | Se(IV), 32.65 ppm + Ref_Calcite solution #1 | $P = 20$ bar, $T = 30$ °C |
| Selenite–Calcite #5 | Se(IV), 48.74 ppm + Ref_Calcite solution #1 | $P = 20$ bar, $T = 30$ °C |
| Selenite–Calcite #6 | Se(IV), 65.54 ppm + Ref_Calcite solution #1 | $P = 20$ bar, $T = 30$ °C |
| Selenate–Calcite #7 | Se(VI), 0.24 ppm + Ref_Calcite solution #1 | $P = 20$ bar, $T = 30$ °C |
| Selenate–Calcite #8 | Se(VI), 16.32 ppm + Ref_Calcite solution #1 | $P = 20$ bar, $T = 30$ °C |
| Selenate–Calcite #9 | Se(VI), 32.65 ppm + Ref_Calcite solution #1 | $P = 20$ bar, $T = 30$ °C |
| Selenate–Calcite #10 | Se(VI), 48.74 ppm + Ref_Calcite solution #1 | $P = 20$ bar, $T = 30$ °C |
| Selenate–Calcite #11 | Se(VI), 65.54 ppm + Ref_Calcite solution #1 | $P = 20$ bar, $T = 30$ °C |
| Se-Cys #12 | Se(-II), 60 ppm + Ref_Calcite solution #1 | $P = 90$ bar, $T = 90$ °C |

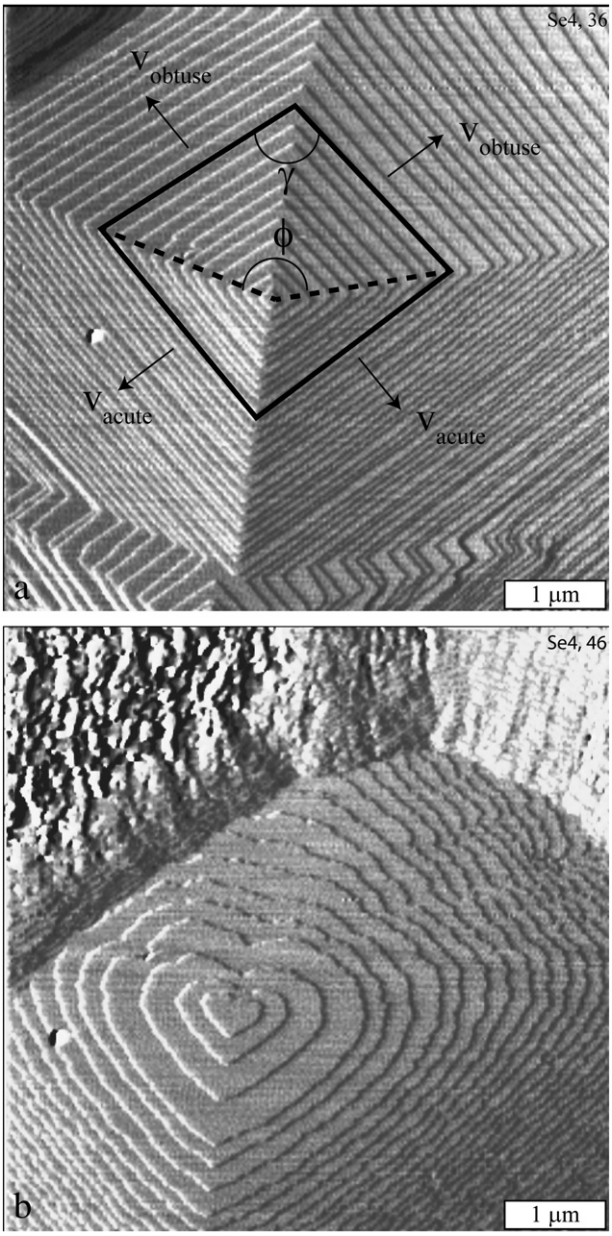


**Fig. 1.** (a) AFM deflection images of spiral growth of a hillock on a $\{10\bar{1}4\}$ calcite cleavage surface, forming a pyramidal form emerging from a screw dislocation. The fluid composition had a ratio $Ca^{2+}/CO_3^{2-}=1$ and a supersaturation equal to 6.45. The pyramid shows obtuse and acute steps that grow with time at a given velocity *v*. The angles ϕ and γ are defined. (b) Same pyramid after injection of 70 ppm Se(IV), showing how the angle γ has been modified, which leads to the formation of a heart-shape pattern. Scale bar: 1 μm.

pressure decreases as the reaction progresses. This pressure drop was visually measured on a manometer as a function of time until the $pCO_2$ reached an equilibrium value in this anisobaric gas–liquid–solid system. This same procedure was used by Montes-Hernandez et al. (2008, 2009, 2011).

At the end of the experiment, the reaction cell was rapidly depressurized over approximately 5 min, followed by disassembly of the autoclave. Twenty milliliters of the suspension were immediately sampled and filtered in order to measure the pH and the selenium concentration which was characterized by inductively coupled plasma atomic emission spectrometry (ICP Perkin Elmer Optima 3300 DV). The amount of selenium present in the solution after the experiment was compared to its initial concentration, with a measurement resolution close to 5% of the initial selenium concentration. The solid product was recovered by centrifuging (30 min at 12,000 rpm) and decanting the supernatant solution. The last step consisted of drying the solid product for 72 h at 65 °C; the recovered material was stored at ambient conditions. In addition to the above conditions, an additional experiment with the same general protocol (using an initial concentration of seleno-L-cystine of 200 mg/L) was carried out at 90 °C and $pCO_2=90$ bar. All experiments carried out in batch reactors are summarized in Table 1. Finally, isolated fine particles (oriented on carbon Ni grids) of some selected samples were visualized using a JEOL 3010 transmission electron microscope (TEM) equipped with an energy dispersive X-ray analyzer (EDS) to image particularly the morphology of calcite crystals precipitated in the absence or in the presence of selenium.

## 3. Results

### 3.1. Effect of selenium during calcite growth: AFM imaging

When water is flowed over a calcite surface, dissolution patterns appear immediately in the form of rhombohedral etch pits that spread until a complete layer of calcite (~0.3 nm) has dissolved. After 5–10 min of dissolution, a pure growth solution (i.e. no selenium) was injected and growth occurred on the freshly dissolved calcite surface. Calcite growth occurs by several modes. Firstly, the etch pits are rapidly filled. Then nucleation of two-dimensional islands occurs more or less randomly over the calcite surface. These molecular steps are approximately 0.3 nm height (one $CaCO_3$ growth layer) and progress laterally over the surface as growth proceeds. They also merge into steps with increasing height. Occasionally, the growth proceeds as hillocks that nucleate at screw dislocations (Fig. 1a). These hillocks have a spiral morphology (pyramidal growth) and we used them to identify four step edges characteristics of growth on the cleavage surface, $\left[\bar{4}41\right]_+$, $\left[48\bar{1}\right]_+$, $\left[\bar{4}41\right]_-$, and $\left[48\bar{1}\right]_-$ (e.g. Ruiz-Agudo et al., 2011). Under normal growth conditions and supersaturation equal to 6.5 and $Ca/CO_3=1$, the average velocity of the steps lies in the range $5.6\pm1.8$ nm $s^{-1}$ for the obtuse steps and $1.5\pm0.7$ nm $s^{-1}$ for the acute steps.

We focused our study on these pyramids, as information regarding step-specific incorporation of selenium on the calcite cleavage plane can be more easily obtained from a detailed study of the morphology and geometry of spiral hillocks. Once one of these features was located, the various selenium forms were added to the growth solutions and injected into the fluid cell (Fig. 3). Under the injection of even small amounts of selenite, the growth pattern of the hillocks significantly changed within minutes. At low selenite concentration (8 ppm), obtuse steps became noticeably scalloped and roughened. Acute steps also became scalloped but to a lesser extent. With increasing selenite concentration, the boundary between the two acute and the two obtuse flanks became indistinguishable and the two obtuse step directions were gradually replaced by a new step direction with edges parallel to the vector $\left[42\bar{1}\right]$ direction, i.e. parallel to the projection of the calcite *c*-glide plane. The pyramid shape evolved towards heart-shaped (Figs. 1b and 4) and tear-shaped patterns (Fig. 3b). Interestingly, when the growth solution was switched to a selenite-free composition, the normal pyramid shape was recovered within a couple of minutes. It was then possible to run cycles of fluid compositions, switching back and forth from “pyramid” to “heart” patterns (see Movie 1 in the Supplementary Material).

In Fig. 5, such alternation of fluid concentration is shown, with the effect on the hillocks: only the presence of selenite significantly modified the morphology of the growth features. When injecting the selenate or the Se–Cys solutions, no significant changes of surface morphology were observed (Fig. 3c–f). In some cases, two edges of

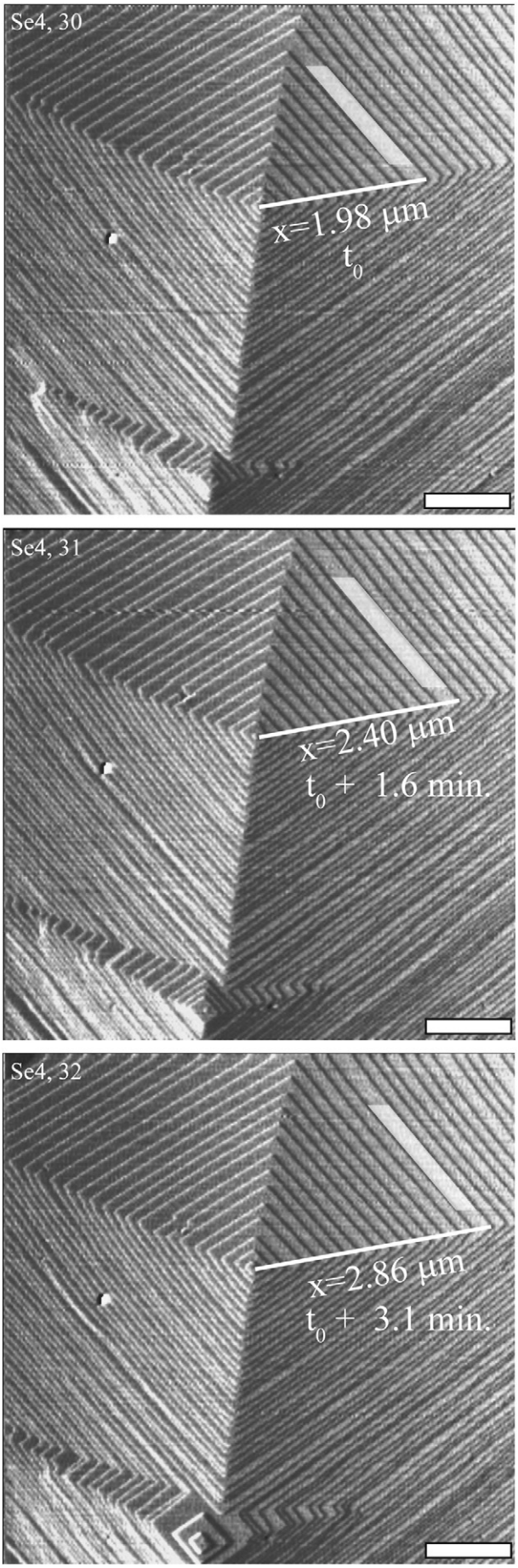


**Fig. 2.** Time-lapse AFM deflection images of a growth hillock. The velocity of growth was measured by following the propagation of a given step, whose distance from the center of the pyramid increased with time. These data are used to calculate the propagation velocity of individual steps (see Eq. (1)). Scale bar: 1 µm.

the pyramidal hillock became more rounded (Fig. 3d). This variation was transient and vanished after a couple of minutes.

Using successive AFM images, the velocity of individual steps was measured by comparing the position of the same step at two different times. The angles $\gamma$ and $\phi$ and the distance $x$ were measured on the images (Fig. 2), and the velocity of the obtuse and acute steps was calculated. The results are shown in Fig. 6 where two effects of selenium on step velocity can be identified. On the one hand, the presence of selenium increased the velocity of obtuse steps by more than 100%. The various selenium forms, selenite, selenate, and Se–Cys, showed this effect up to a concentration of 70 ppm. On the other hand, the presence of selenate and Se–Cys slightly increased the velocity of the acute steps, while selenite did not affect the rate of acute step spreading (within the error of the measurements).

### 3.2. Effect of selenium during calcite growth: batch reactor experiments

Fig. 7, with data from the ICP measurements, shows that a high proportion of initial selenite oxyanion in the system was sequestered during calcite growth: more than 80% of the selenite initially present in the solution was incorporated into calcite crystals. No other solid phases could be detected in the reaction products, neither from TEM images, nor in X-ray diffraction (EXD) analyses. TEM images (insets in Figs. 7 and 8) reveal that the presence of selenite oxyanion during calcite growth results in a *c*-axial elongation of rhombohedral crystals. Conversely, the selenate oxyanion had insignificant physicochemical affinity during calcite formation. Moreover, no change of crystal morphology was observed at the microscopic scale (inset in Fig. 7).

TEM measurements on calcite revealed a very complex effect of seleno-L-cystine on the particle size and the aggregation-agglomeration process. Several types of morphologies were observed such as rhombohedra, elongated rhombohedra (*c*-axis elongation), scalenohedra, star-like crystal aggregates, and irregular calcite polycrystals – see Fig. 8b and the TEM measurements reported in Montes-Hernandez et al. (2011).

## 4. Discussion

### 4.1. Incorporation of selenium and effect on calcite growth

The experiments reported in this study confirm, by direct observation, that under the chosen thermodynamic conditions, selenate is not incorporated into calcite during growth, whereas selenite is incorporated. This has already been shown in a previous study where EXAFS spectroscopy was used (Montes-Hernandez et al., 2011). However AFM enables the mechanism of interaction and incorporation to be more fully understood. Roughening and rounding of obtuse and acute step edges is the morphologic manifestation of the incorporation of selenium ions. Instead of forming linear steps, the incorporation of selenite induces some local misalignment, leading to a less regular growth of the obtuse steps (arrows in Fig. 4c). Moreover, step and island morphologies on a growing mineral surface, observed using AFM, typically are reflected in the micro and macroscopic form of the crystal (e.g. Kowacz and Putnis, 2008; Ruiz-Agudo et al., 2010). Thus, the observed elongation of the growth hillock in the presence of Se (IV) (AFM images, Fig. 4) is connected with the *c*-axial elongation of rhombohedra crystals formed in batch experiments (TEM images, Fig. 8).

The question may arise as to the exact mechanism of selenite adsorption or incorporation on the calcite surface. On the one hand, the AFM images show that there is no co-precipitate of a selenium-rich

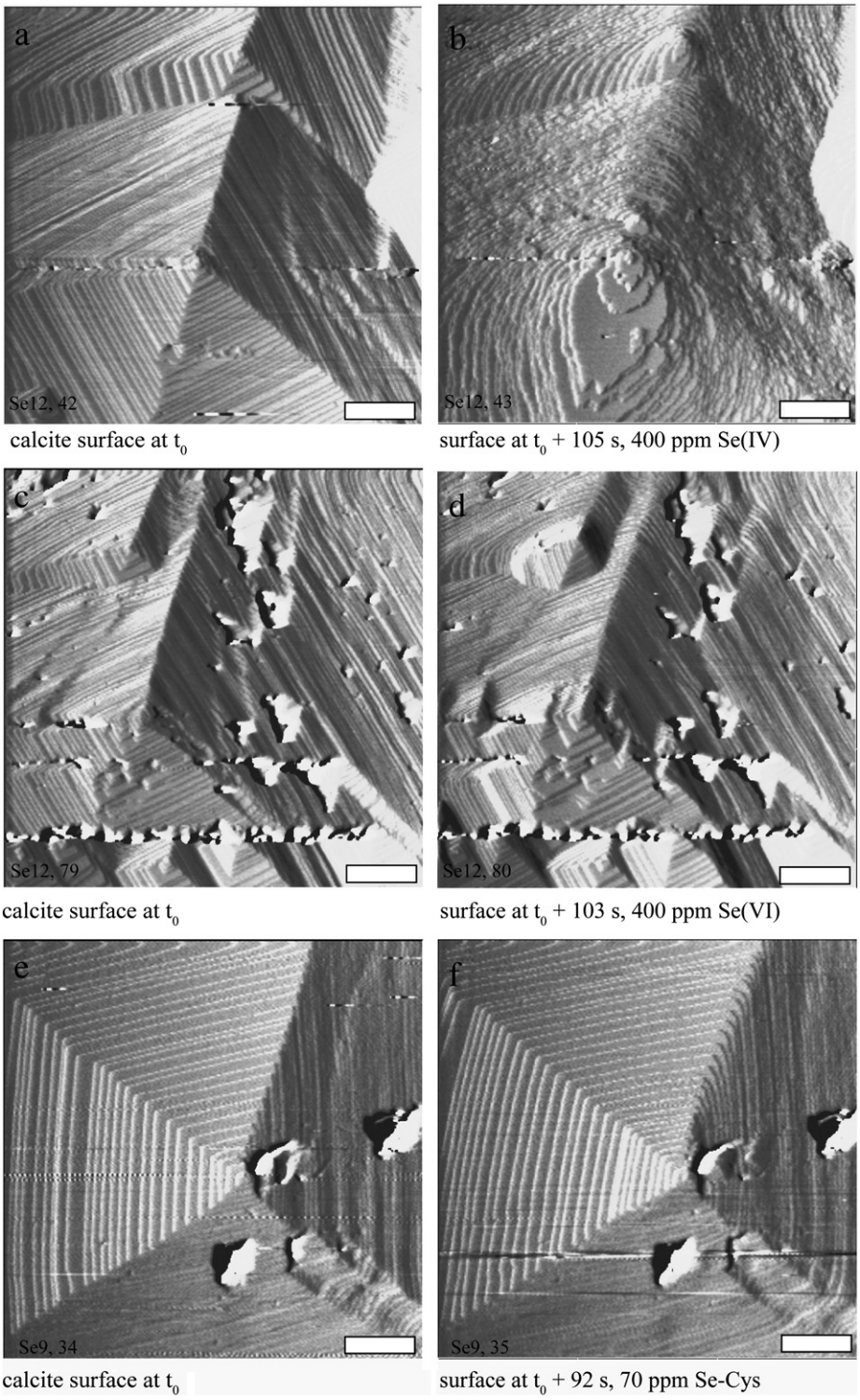


**Fig. 3.** AFM images of the effect of adding aqueous solutions containing the various forms of selenium on a calcite surface during growth. (a and b) Addition of 200 ppm of selenite, Se(IV) and immediate roughening of the surface, elongation of the pyramid apex leading to the formation of a tear-shape pattern. (c and d) Addition of 400 ppm selenate, Se(VI), showing no significant effect on the morphology of the pyramid. (e and f) Addition of 70 ppm Se–Cys showing no significant effect on the morphology of the pyramid, apart from the observation that one of the edges of the pyramid became slightly rounded. Scale bar: 1 μm.

phase on the calcite surface. As well, we found no evidence in our AFM study for Se incorporation in non-structural sites, as we would expect to observe a higher step thickness in the newly grown calcite, as a result of the anomalous deformation of the $\{10\bar{1}4\}$ planes (Astilleros et al., 2000). All in all, this suggests that selenite must be incorporated into the crystalline structure of calcite, as also witnessed by the large amount of Se(IV) incorporated into calcite in the batch reactions. The thermochemical radius of the carbonate ion (0.178 nm) is smaller than that of selenite (0.239 nm) and selenate (0.249 nm) (Jenkins and Thakur, 1979), see also Fig. 5. The selenate $SeO_4^{2-}$ ion has a tetrahedral shape, whereas the selenite ion $SeO_3^{2-}$ is trigonal pyramidal with a flat shape. As a result, the incorporation of selenite should be easier but nevertheless it should also distort the cell structure of calcite

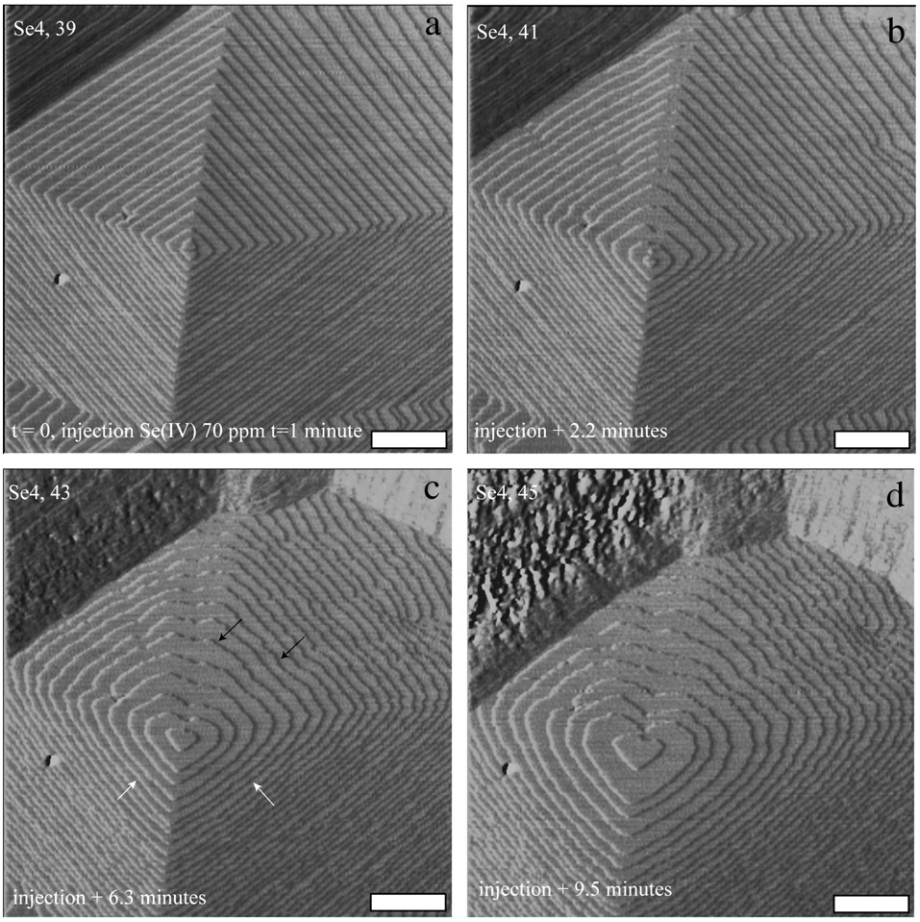


**Fig. 4.** Time-lapse AFM deflection images of a spiral hillock that grew in the presence of selenite at a concentration of 70 ppm. The presence of selenite had two effects: the shape of the pyramid evolved towards a heart-shape pattern and the surface of calcite at the top left corner became rougher. Scale bar: 1 μm. White arrows point to acute steps; black arrows indicate how the initially linear obtuse steps become rough.

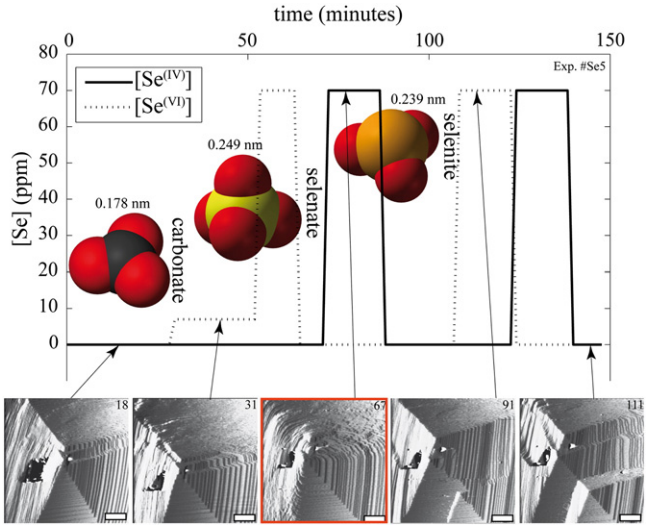


**Fig. 5.** Time-lapse AFM deflection images of a hillock that grew in the presence of various concentrations of selenium: selenate 8 ppm and 70 ppm (dashed curve), selenite 70 ppm (plain curve). In the presence of selenite only (central AFM image), the spiral growth of the pyramid was perturbed. Selenate had no measurable effect at these two concentrations. Interestingly, every time the injected growth solution did not contain selenite, the pyramidal shape pattern recovered its original shape within less than 3 min. Scale bar: 1 μm. The three oxyanions are represented (oxygen atoms in red) and their thermochemical radius (Jenkins and Thakur, 1979) is indicated.

because of its larger radius, as proposed by Montes-Hernandez et al. (2011). Since the charge on selenite and selenate is the same (−2), we could postulate that an important parameter could be bond valence. The average bond valence of C–O bonds in carbonate and Se–O bonds in selenite is 1.33 valence units, whereas the average Se–O bond valence in selenate is 1.5 valence units. Since all three of the oxygen atoms in the carbonate groups are bonded equally, with one C–O bond of about 1.33 valence unit and two Ca–O bonds of about 0.33 valence unit, the accommodation of another 0.17 valence unit on each C–O bond in the case of selenate incorporation would induce a strong distortion of the CaO6 octahedra. Thus the incorporation of selenite on a carbonate substitution site would be structurally favored over selenate.

One can also consider the distances between atoms in the various configurations. The Se(IV) has a lone pair, so it is trigonal pyramidal, and not trigonal planar as $CO_3$. The lone pair repels the bonded pairs, so that the O–Se–O angles are less than 100°, as opposed to the ideal tetrahedral angle of 109.5°. As a consequence, it would force the O atoms closer together, so that the O–O distances would be about 2.55 Å in selenite, compared to a 2.24 Å O–O distance in calcite carbonate groups. The O–O distance in selenate is close to 2.65 Å, making it more difficult to bond the oxygen atoms of this anion with calcium. The lone pair distortion might also explain why the crystals incorporating selenite would elongate in the c-direction. The 3-fold axes of the carbonate groups are all parallel to the c-direction, so if selenite is incorporated in those sites there would be extra repulsion between the lone pair and other O atoms in the c-direction.

Thus, to summarize, the selenite oxyanion, $SeO_3^{2-}$, has the same electronic charge and closer dimensions to the carbonate group than

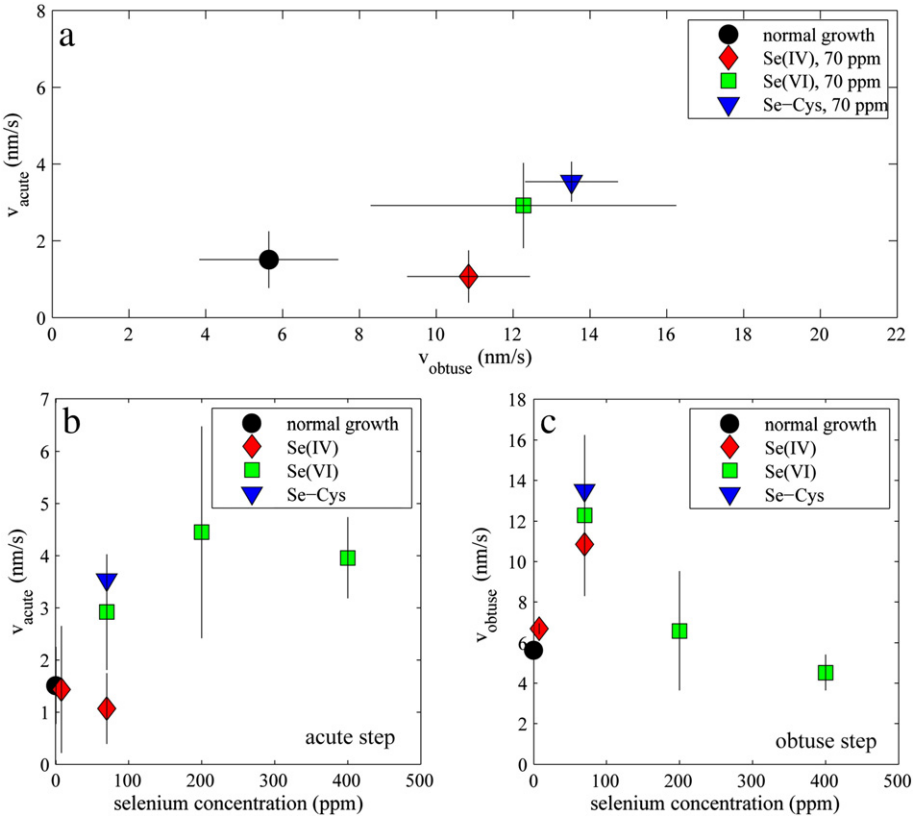


**Fig. 6.** Velocity of obtuse and acute steps in AFM experiments. (a) Average step velocities and standard deviation for selenium concentrations of 70 ppm. The average behavior is that Se(VI) and Se–Cys induced an increase of the velocity of both steps. For Se(IV), the velocity of the obtuse steps increased, whereas the velocity of the acute steps was reduced, leading to the formation of the heart-shape pattern. (b) Velocity of acute steps as a function of selenium concentration. (c) Velocity of the obtuse steps as a function of selenium concentration. Error bars in step velocities are determined by measuring the rate of propagation of 5–10 steps and calculating the standard deviation.

selenate. Therefore a substitution with the carbonate group is more likely than a substitution of the carbonate group by $SeO_4^{2-}$ with a different geometry and valence, which would distort to a greater extent the calcite structure. This process has already been discussed (Reeder et al., 1994; Alexandratos et al., 2007; Tang et al., 2007; Aurelio et al., 2010) and increasingly more reliable measurements using, for example

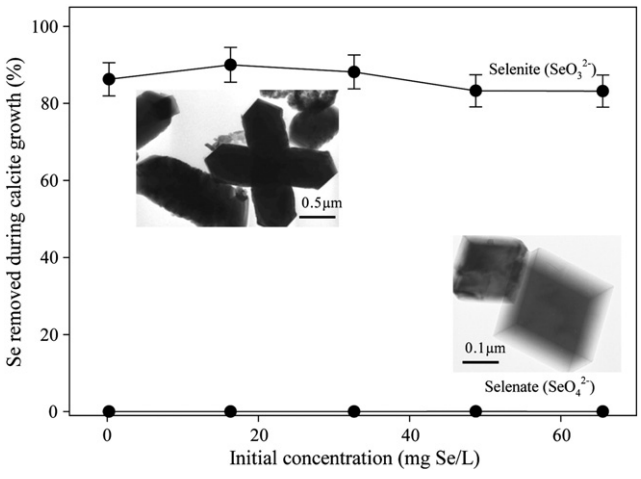


**Fig. 7.** Incorporation of selenium in batch reactor experiments during the precipitation of calcite from a slurry of portlandite, water and carbon dioxide. For selenite, the percentage of incorporation into calcite was always larger than 80%, for initial concentrations in the solution in the range 0.24–65.5 ppm Se. For selenate, the incorporation was negligible. Errors in the measurements are close to 5% of the initial selenium concentration in the solution. Transmission electron images of the produced calcite crystals in the presence of selenate or selenite are displayed in insets.

synchrotron X-ray adsorption spectroscopy, have demonstrated that selenite is incorporated into the calcite structure, substituting the carbonate on a single site (Montes-Hernandez et al., 2011). The possibility of adsorption of selenite on other surface sites has not been ruled out, particularly at high selenium concentrations. This adsorption process could be responsible for the roughening of the calcite surface observed in the AFM images, where selenite molecules would prevent the calcite steps from growing smoothly by allowing widespread nucleation of a large number of new steps. For the selenate molecule, no incorporation was measured in the batch reactions. Nevertheless, adsorption on a calcite surface cannot be ruled out. However, if it exists, it does not seem to modify the growth mechanism, and only increases the growth rate.

Finer scalloping along obtuse step edges may be indicative of more closely spaced selenite oxyanions along those step edges, which would suggest higher Se content in obtuse rather than in acute step edges of the growth spirals on the growing calcite surface. Thus, our AFM observations suggest that $SeO_3^{2-}$ selectively interacts with calcite growth steps and give indirect evidence for the preferential incorporation of this species at obtuse steps. From a structural point of view, it seems reasonable to think that $SeO_3^{2-}$ species will fit better in a less constrained space, as they are larger than carbonate ions. Also, the observed changes in spiral hillock shape, particularly the elongation along the $\left[4\bar{2}1\right]$ direction, may be related to stabilization of $\left\{01\bar{1}2\right\}$ faces by adsorption of Se oxyanions. $\left\{01\bar{1}2\right\}$ are polar faces (i.e. there is a net dipole moment perpendicular to such faces) and thus they are not stable under normal growth conditions (nucleation from pure solutions). Similar findings have been observed in the presence of organic additives (Ruiz-Agudo et al., 2010).

In this study, one effect of the various forms of selenium on the calcite growth rate is to increase the rates of step spreading. Several

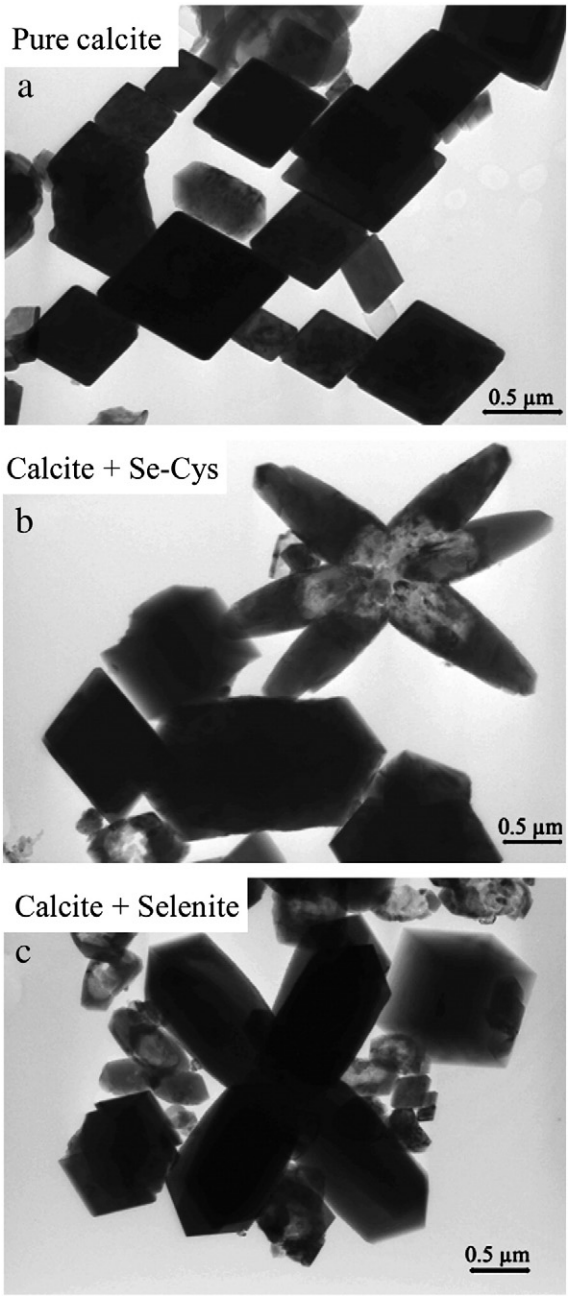


**Fig. 8.** Transmission electron microscopy (TEM) images of calcite crystals precipitated from $Ca(OH)_2$–$H_2O$–$CO_2$ slurry in a batch reactor. In the presence of selenite or seleno-L-cystine (Se–Cys), the crystal morphology changed from typical rhombohedral crystals (a) to crystals that show axial elongation (b and c) and aggregation into star-like morphologies.

processes have been proposed to explain why impurities may modify the kinetics of step development (Davis et al., 2000; De Yoreo et al., 2009). Step rate at constant temperature may be controlled by several factors such as step-edge kink site availability, solute flux and composition, or complexation of the cation (Morse et al., 2007; Wolthers et al., 2012). For the advance of straight steps such as those on polygonized spirals observed here, kink availability and dehydration of the cation are most likely the limiting factors as the solution was continuously renewed.

A possible explanation could be that the adsorption of selenium oxyanions at steps creates kinks or promotes attachment sites for $Ca^{2+}$ and $CO_3^{2-}$ ions. For the case of the selenate anion, the adsorption is likely to be weak because of the geometric incompatibility of selenate. Ultimately, upon the attachment of $Ca^{2+}$ and $CO_3^{2-}$, the selenate anions may desorb and recycle in the step growth process, whereas for selenite this process can also lead to the incorporation of this anion into the step. To test such ideas, molecular dynamics simulations (Kerisit and Parker, 2004) would be necessary to estimate the free energy barriers for anion incorporation during the different steps of this process.

An alternative explanation would be to consider that the presence of these impurity anions may increase the growth rate by increasing the rate of cation (calcium) attachment, which is considered to be the rate-limiting step for calcite growth. Anions present in solution may modify calcium hydration in solution and/or assist the attachment of calcium to the growing surface (see for example Ruiz-Agudo et al., 2011; Wolthers et al., 2012). Both of these effects will affect the frequency of attachment of building units ($Ca^{2+}$ and $CO_3^{2-}$) to the crystal surface, and therefore, the kinetics of crystal growth.

The observed effects on growth morphology and kinetics are not due to the state of selenium protonation or complexation in the fluid. Thermodynamic simulations using PHREEQC (Parkhurst and Appelo, 1999) indicate that at the pH of the experiments (pH ~8), more than 96% of the selenium is not protonated or does not form a complex with calcium: $SeO_3^{2-}$ or $SeO_4^{2-}$ ions are therefore the dominant species.

Finally, an intermediate behavior between Se(IV) and Se(VI) was observed in the case for organically bonded selenium. Here, our interpretation is that the Se–Cys molecule must partly dissociate in solution, leading to the formation of free selenium and organic molecules (acid and amine groups of Se–Cys). The Se–Cys molecule was not chemically stable during calcite growth; it would most likely have been chemically fragmented since the selenium would have been oxidized from Se(−II) (in seleno-L-cystine) to Se(0) and Se(IV) under $O_2$-poor conditions, and to Se(0), Se(IV) and Se(VI) under $O_2$-rich conditions (see also Montes-Hernandez et al., 2008). The fate of the remaining organic residue during calcite growth is unclear. EXAFS measurements using linear combination fits have only revealed that Se–Cys was present in the solid product at low temperature (30 °C), see Fig. 8 by Montes-Hernandez et al. (2011). Moreover, in a previous study, HPLC coupled to ICP-MS was used to measure the residual Se–Cys in solution during the carbonation process. This revealed a rapid consumption of Se–Cys, and no more was detected after 1 h of reaction when the temperature was fixed at 90 °C (see Table 1 in Montes-Hernandez et al., 2008). However, the residual organic groups (amine and acid) may be responsible for the star-like aggregates because these morphologies were not observed when calcite was grown in the presence of selenite oxyanions.

### *4.2. Implication for selenium mobility in geological environments*

Selenium can be found in various oxidation states in natural environments: Se(−II) in a reducing environment such as sediments in some lakes; Se(0) the elemental form of selenium; in oxidizing environments Se(IV) and Se(VI) are present in forms of oxyanions, $SeO_3^{2-}$ and $SeO_4^{2-}$ respectively, with a high bioavailability and bioaccumulation potential. Selenium mobility in the upper crust and soils and its solubility in waters are controlled by the redox potential and pH, the strong sorption in soils by hydroxides, and the uptake by plants where selenium binds in organic molecules (Mayland et al., 1989). In sea and oceanic waters, the concentration of Se(IV) is usually several times smaller than Se(VI), indicating that the later is more mobilized than the former (Table 2 in Conde and Sanz Alaejos, 1997). Conversely other examples of selenium oxidation state analyses in various fresh water environments indicate the domination of either the Se(IV) species in rain waters or the Se(VI) species in rivers, groundwater and snow – see the extensive review by Conde and Sanz Alaejos (1997) who collected dozens of analyses of selenium concentrations in various kinds of

**Table 2**
Composition of the solutions used for AFM studies, pH, supersaturation (Ω), and activity coefficients of calcium and carbonate. The concentration of selenium (ppm) is also given.

| Selenite Se [ppm] | $Na_2SeO_3$ $\times 10^{-3}$ M | $CaCl_2$ $\times 10^{-3}$ M | $NaHCO_3$ $\times 10^{-3}$ M | pH | Ω | $aCa^{2+}$ $\times 10^{-4}$ | $aCO_3^{2-}$ $\times 10^{-4}$ | $aCa^{2+}/aCO_3^{2-}$ |
|---|---|---|---|---|---|---|---|---|
| 0,8 | 0.01 | 0.33 | 25.15 | 8.18 | 6.46 | 1.38 | 1.38 | 1.00 |
| 4 | 0.05 | 0.33 | 25.03 | 8.18 | 6.46 | 1.38 | 1.38 | 1.00 |
| 8 | 0.10 | 0.34 | 24.89 | 8.19 | 6.46 | 1.38 | 1.38 | 1.00 |
| 39 | 0.50 | 0.37 | 23.78 | 8.21 | 6.46 | 1.38 | 1.38 | 1.00 |
| 70 | 0.76 | 0.40 | 23.09 | 8.21 | 6.46 | 1.38 | 1.38 | 1.00 |
| 200 | 2.50 | 0.55 | 19.13 | 8.21 | 6.46 | 1.38 | 1.38 | 1.00 |
| 400 | 5.00 | 0.78 | 15.26 | 8.21 | 6.46 | 1.38 | 1.38 | 1.00 |
| Selenate Se [ppm] | $Na_2SeO_4$ $\times 10^{-3}$ M | $CaCl_2$ $\times 10^{-3}$ M | $NaHCO_3$ $\times 10^{-3}$ M | pH | Ω | $aCa^{2+}$ $\times 10^{-4}$ | $aCO_3^{2-}$ $\times 10^{-4}$ | $aCa^{2+}/aCO_3^{2-}$ |
| 0.8 | 0.01 | 0.33 | 25.18 | 8.18 | 6.46 | 1.38 | 1.38 | 1.00 |
| 4 | 0.05 | 0.33 | 25.21 | 8.18 | 6.46 | 1.38 | 1.38 | 1.00 |
| 8 | 0.10 | 0.33 | 25.25 | 8.18 | 6.46 | 1.38 | 1.38 | 1.00 |
| 39 | 0.50 | 0.35 | 25.52 | 8.18 | 6.46 | 1.38 | 1.38 | 1.00 |
| 70 | 0.76 | 0.36 | 25.69 | 8.18 | 6.46 | 1.38 | 1.38 | 1.00 |
| 200 | 2.53 | 0.43 | 26.80 | 8.18 | 6.46 | 1.38 | 1.38 | 1.00 |
| 400 | 5.07 | 0.52 | 28.23 | 8.18 | 6.46 | 1.38 | 1.38 | 1.00 |
| Se-Cys Se [ppm] | | $CaCl_2$ $\times 10^{-3}$ M | $NaHCO_3$ $\times 10^{-3}$ M | pH | Ω | $aCa^{2+}$ $\times 10^{-4}$ | $aCO_3^{2-}$ $\times 10^{-4}$ | $aCa^{2+}/aCO_3^{2-}$ |
| 70 | | 0.36 | 25.69 | 8.18 | 6.46 | 1.38 | 1.38 | 1.00 |

waters. Several causes could explain the distribution of the various selenium ions, including the local pH and redox potential or the presence of humic acids that binds preferentially with Se(IV). In the present study, we propose an additional effect: the preferential incorporation of Se(IV) into calcite, effectively removing it from solution, and therefore could explain the higher concentrations of Se(VI) measured in various natural waters. This proposition should, however, be confirmed by extensive analyses of the chemical composition of limestones and natural calcite crystals worldwide. However, to our knowledge, such a chemical database is not available.

## 5. Conclusion

Based on AFM imaging and batch reaction measurements, our data indicate that selenium may interact with calcite during its growth.

1 At room temperature and concentrations of selenium in the range 1–400 ppm, selenite incorporates into calcite, while selenate does not incorporate. This is most likely due to the shape and size of the $SeO_3^{2-}$ selenite ion (flat trigonal pyramid, similar dimensions, same electronic charge) that can replace the carbonate group $CO_3^{2-}$.
2 The incorporation of selenite at concentrations up to 70 ppm is almost total. $SeO_3^{2-}$ preferentially interacts with calcite obtuse growth steps. The incorporation modifies the morphology of the steps at the growing calcite surface; at the microscopic scale this induces an axial elongation of the calcite crystals.
3 The rate of obtuse step propagation at the calcite surface is increased by the presence of both selenite and selenate. However, the acute step propagation is inhibited by the presence of selenite, giving the pyramidal hillocks a heart-shape pattern.

Supplementary data to this article can be found online at http://dx.doi.org/10.1016/j.chemgeo.2012.12.017.

## Acknowledgements

G. Montes-Hernandez is grateful to ANR French research agency for providing a financial support (ANR CORO project). E. Ruiz-Agudo acknowledges the Spanish Ministry of Economy and Competitiveness for a Ramón y Cajal Grant as well as additional funding provided by the research group RNM-179 (Junta de Andalucía, Spain). The experimental facilities in the Institut für Mineralogie, University of Münster, are supported by the German Research Council (DFG). We also thank two anonymous reviewers for constructive comments and for pointing to us alternative interpretations of our results.

## References

Alexandratos, V.G., Elzinga, E.J., Reeder, R.J., 2007. Arsenate uptake by calcite: macroscopic and spectroscopic characterization of adsorption and incorporation mechanisms. Geochimica et Cosmochimica Acta 71, 4172–4187.
Astilleros, J.M., Pina, C.M., Fernández-Díaz, L., Putnis, A., 2000. The effect of barium on calcite (10–14) surfaces during growth. Geochimica et Cosmochimica Acta 64, 2965–2972.
Aurelio, G., Fernandez-Martinez, A., Cuello, G.J., Roman-Ross, G., Alliot, I., Charlet, L., 2010. Structural study of selenium (IV) substitutions in calcite. Chemical Geology 270, 249–256.
Bischof, J.L., 1968. Kinetic of calcite nucleation: magnesium ion inhibition and ionic strength catalysis. Journal of Geophysical Research 73, 3315–3322.
Cheng, L., Lyman, P.F., Sturchio, N.C., Bedzyk, M.J., 1997. X-ray standing wave investigation of the surface structure of selenite anions adsorbed on calcite. Surface Science 382, L690–L695.
Conde, J.E., Sanz Alaejos, M., 1997. Selenium concentrations in natural and environmental waters. Chemical Reviews 97, 1979–2003.
Davis, K.J., Dove, P.M., De Yoreo, J.J., 2000. The role of $Mg^{2+}$ as an impurity in calcite growth. Science 290, 1134–1137.
De Yoreo, J.J., Zepeda-Ruiz, L.A., Friddle, R.W., Qiu, S.R., Wasylenki, L.E., Chernov, A.A., Gilmer, G.H., Dove, P.M., 2009. Rethinking classical crystal growth models through molecular scale insights: consequences of kink-limited kinetics. Crystal Growth and Design 9, 5135–5144.
Dove, P.M., Hochella, J.R.M.F., 1993. Calcite precipitation mechanisms and inhibition by orthophosphate: in situ observation by scanning force microscopy. Geochimica et Cosmochimica Acta 57, 705–714.
Draize, J.H., Beath, O.A., 1935. Observations on the pathology of blind staggers and alkali disease. American Veterinary Medicine Association Journal 86, 753–763.
Ellis, M.M., Motley, H.L., Ellis, M.D., Jones, R.O., 1937. Selenium poisoning in fishes. Proceedings of the Society for Experimental Biology and Medicine 36, 519–522.
EC Scientific Committee on Food, 2003. Opinion of the Scientific Committee on Food on the Revision of Reference Values for Nutrition Labelling. Commission of the European Communities, Brussels.
Fernandez-Martinez, A., Charlet, L., 2009. Selenium bioavailability and cycling in the environment: a structural chemist's point of view. Reviews in Environmental Science and Biotechnology 8, 81–110.
Floor, G.H., Román-Ross, G., 2012. Selenium in volcanic environments: a review. Applied Geochemistry 27, 517–531.
Fujita, Y., Redden, G.D., Ingram, J., Cortez, M.M., Ferris, G., Smith, R.W., 2004. Strontium incorporation into calcite generated by bacterial ureolysis. Geochimica et Cosmochimica Acta 68, 3261–3270.
Hamilton, S.J., 2004. Review of selenium toxicity in the aquatic food chain. Science of the Total Environment 326, 1–31.
Hay, M.B., Workman, R.K., Manne, S., 2003. Mechanisms of metal ion sorption on calcite: composition mapping by lateral force microscopy. Langmuir 19, 3727–3740.
Heberling, F., Denecke, M.A., Bosbach, D., 2008. Neptunium(V) coprecipitation with calcite. Environmental Science and Technology 42, 471–476.

Jenkins, H.B.D., Thakur, K.P., 1979. Reappraisal of thermochemical radii for complex ions. Journal of Chemical Education 56, 576–577. http://dx.doi.org/10.1021/ed056p576.
Kerisit, S., Parker, S.C., 2004. Free energy of adsorption of water and metal ions on the 10–14 calcite surface. Journal of the American Chemical Society 126, 10152–10161.
Kowacz, M., Putnis, A., 2008. The effect of specific background electrolytes on water structure and solute hydration: consequences for crystal dissolution and growth. Geochimica and Cosmochimica Acta 72, 4476–4487.
Larsen, K., Bechgaard, K., Stipp, S.L.S., 2010. The effect of the $Ca^{2+}$ to $CO_3^{2-}$ activity ratio on spiral growth in the calcite $\{10\bar{1}4\}$ surface. Geochimica et Cosmochimica Acta 74, 2099–2109.
Lee, Y.J., Reeder, R.J., 2006. The role of citrate and phthalate during Co(II) coprecipitation with calcite. Geochimica et Cosmochimica Acta 70, 2253–2263.
Levander, O.A., Burk, R.F., 2006. Update of human dietary standards for selenium. Its molecular biology and role in Human Health. Springer, US, New York, pp. 399–410.
Li, S., Zhao, L., 2007. Geochemistry and origin of lead and selenium in the no. 6 coal from the Junger coalfield, North China. Energy Exploration & Exploitation 25, 175–183.
Malisa, E.P., 2001. The behaviour of selenium in geological processes. Environmental Geochemistry and Health 23, 137–158.
Mayland, H.F., James, L.F., Panter, K.E., Sonderegger, J.L., 1989. In *Selenium in Agriculture and the Environment*. Soil Science Society of America and American Society of Agronomy, Special Publication 23, 15–48.
Montes-Hernandez, G., Fernandez-Martinez, A., Charlet, L., Renard, F., Scheinost, A.C., Bueno, M., 2008. Synthesis of a $Se^0$/calcite composite using hydrothermal carbonation of $Ca(OH)_2$ coupled to a complex selenocystine fragmentation. Crystal Growth and Design 8, 2497–2504.
Montes-Hernandez, G., Concha-Lozano, N., Renard, F., Quirico, E., 2009. Removal of oxyanions from synthetic wastewater via carbonation process of calcium hydroxide: applied and fundamental aspects. Journal of Hazardous Materials 166, 788–795.
Montes-Hernandez, G., Sarret, G., Hellmann, R., Menguy, N., Testemale, D., Charlet, L., Renard, F., 2011. Nanostructured calcite precipitated from $CO_2$-$H_2O$-$Ca(OH)_2$ medium in presence of selenium inorganic/organic impurities. Chemical Geology 290, 109–120.
Morse, J.W., Arvidson, R.S., Lüttge, A., 2007. Calcium carbonate formation and dissolution. Chemistry Review 107, 342–381.
Nancollas, G.H., Reddy, M.M., 1971. The crystallization of calcium carbonate II: calcite growth mechanism. Journal of Colloid and Interface Science 37, 824–830.
Paquette, J., Reeder, R.J., 1995. Relationship between surface structure, growth mechanism, and trace element incorporation in calcite. Geochimica et Cosmochimica Acta 59, 735–749.
Parkhurst, D.L., Appelo, C.A.J., 1999. Users guide to PHREEQC (version 2) – A computer program for speciation, batch reaction, one dimensional transport, and inverse geochemical calculations. US Geological Survey Water-Resources Investigation Report 99–4259 (312 pp.).
Reeder, R.J., Lamble, G.M., Lee, J.-F., Staudt, W.J., 1994. Mechanism of $SeO_4^{2-}$ substitution in calcite: an XAFS study. Geochimica et Cosmochimica Acta 58, 5639–5646.
Rouxel, O., Fouquet, Y., Ludden, J.H., 2004. Subsurface processes at the Lucky Strike hydrothermal field, Mid-Atlantic ridge: evidence from sulfur, selenium and iron isotopes. Geochimica et Cosmochimica Acta 10, 2295–2311.
Ruiz-Agudo, E., Putnis, C.V., 2012. Direct observations of mineral-fluid reactions using atomic force microscopy: the specific example of calcite. Mineralogical Magazine 76, 227–253.
Ruiz-Agudo, E., Di Tommaso, D., Putnis, C.V., de Leeuw, N.H., Putnis, A., 2010. Interactions between organophosphonate-bearing solutions and 1014 calcite surfaces: an AFM and first principles molecular dynamics study. Crystal Growth and Design 10, 3022–3035.
Ruiz-Agudo, E., Putnis, C.V., Wang, L., Putnis, A., 2011. Specific effects of background electrolytes on the kinetics of step propagation during calcite growth. Geochimica et Cosmochimica Acta 75, 3803–3814.
Saldi, G.D., Jordan, G., Schott, J., Oelkers, E.H., 2009. Magnesite growth rates as a function of temperature and saturation state. Geochimica et Cosmochimica Acta 76, 5646–5657.
Staudt, W.J., Reeder, R.J., Schoonen, M.A.A., 1994. Surface structural controls on compositional zoning of $SO_4^{2-}$ and $SeO_4^{2-}$ in synthetic calcite single crystals. Geochimica and Cosmochimica Acta 58, 2087–2098.
Stipp, S.L.S., Christensen, J.T., Lakshtanov, L.Z., Baker, J.A., Waight, T., 2006. Rare Earth element (REE) incorporation in natural calcite: upper limits for actinide uptake in a secondary phase. Radiochimica Acta 94, 523–528.
Tang, Y., Elzinga, E.J., Lee, Y.L., Reeder, R.J., 2007. Coprecipitation of chromate with calcite: batch experiments and X-ray absorption spectroscopy. Geochimica et Cosmochimica Acta 71, 1480–1493.
Temman, M., Paquette, J., Vali, H., 2000. Mn and Zn incorporation into calcite as a function of chloride aqueous concentration. Geochimica et Cosmochimica Acta 64, 2417–2430.
Teng, H.H., Dove, P.M., Orme, C.A., De Yoreo, J.J., 1998. Thermodynamics of calcite growth: baseline for understanding biomineral formation. Science 282, 724–727.
Wolthers, M., Nehrke, G., Gustafsson, J.P., van Cappellen, P., 2012. Calcite growth kinetics: modeling the effect of solution stoichiometry. Geochimica et Cosmochimica Acta 77, 121–134.
Yudovich, Y.E., Ketris, M.P., 2006. Selenium in coal: a review. International Journal of Coal Geology 67, 112–126.